Effects of the Tool Microgeometry on Thermo-Mechanical Loads for Ti-6Al-4V Finishing Cutting Operations

Matthieu Paillard, Frédéric Rossi, Hélène Elias-Birembaux, Gérard Poulachon, Mathieu Ritou, Nicolas Maury

Available online at www.sciencedirect.com

ScienceDirect

Procedia CIRP 133 (2025) 442–447

www.elsevier.com/locate/procedia

20th CIRP Conference on Modeling of Machining Operations

Effects of the Tool Microgeometry on Thermo-Mechanical Loads for Ti-6Al-4V Finishing Cutting Operations

Matthieu PAILLARD [a, b], Frédéric ROSSI [a], Hélène ELIAS-BIREMBAUX [a], Gérard POULACHON [a], Mathieu RITOU [c], Nicolas MAURY [b]

[a] *Arts et Metiers Institute of Technology, LABOMAP, Université Bourgogne Franche-Comté, F-71250 Cluny, France*
[b] *Airbus Operations SAS, 31200 Toulouse, France*
[c] *Nantes Université, LS2N, 44000 Nantes, France*

* Corresponding author. *E-mail address:* matthieu.paillard@ensam.eu

Abstract

Achieving a high-quality surface while minimizing the adverse effects associated with machining operations, particularly in finishing processes, is a major challenge in aerospace component manufacturing. To overcome the limitations of conventional numerical simulations of cutting operations, which involve chip formation and complex contact management, this paper proposes a simplified approach to model the thermal loading generated during cutting using a chipless method. After analytically determining the effort-based thermal sources and validating the chipless model, the influence of tool microgeometry on thermo-mechanical loading is investigated emphasizing this parameter as an important factor for finishing cutting operations.

Peer-review under responsibility of the scientific committee of the 20th CIRP Conference on Modeling of Machining Operations in Mons

Keywords: Tool microgeometry; Thermo-mechanical loads; Orthogonal Cutting; Ti-6Al-4V; Chipless modeling; Hybrid modeling

1. Introduction

Machining processes are essential in the production of high-value-added components, such as those used in the aerospace industry. A distinction can be made between finishing and roughing operations, with the first involving significantly lower chip thicknesses. As suggested by Denkena et al. [1] and Zhuang et al. [2], tool microgeometry affects material flow around the cutting edge and, consequently, the thermo-mechanical load generated as it passes through the workpiece. While a sharp edge tends to facilitate cutting, a chamfered or honed edge is more likely to induce ploughing and/or flank friction. This observation is supported by Wyen et al.'s study [3] on orthogonal cutting tests of Ti-6Al-4V, where they correlate increases in specific cutting forces with an increase in tool edge radius. Thrust forces are most influenced by edge microgeometry, which in turn impacts thermal behavior by increasing the tool/workpiece contact length, friction intensity, and the deformation energy dissipated during ploughing. Several authors have investigated these phenomena. Segebade et al. [4] demonstrate through a numerical study of Ti-6Al-4V machining that honed microgeometries have a greater thermal impact than rounded microgeometries. Similar observations were made by Denkena et al. [5], who, using a two-color pyrometer, identified predominant effects of the lower part of the cutting edge in generating heat at the tool tip during machining of AISI 1045. Using an IR-CCD camera system, M'Saoubi et al. [6] also showed an increase in tool-tip

Peer-review under responsibility of the scientific committee of the 20th CIRP Conference on Modeling of Machining Operations in Mons
10.1016/j.procir.2025.02.076

temperature when machining steel with a worn or rounded tool. These studies highlight tool microgeometry as a critical parameter for accurately modeling thermo-mechanical loads, thereby enabling more precise predictions of surface integrity.

Building on the historical models by Waldorf et al. [7] and Komanduri et al. [8] to simulate edge forces and thermal sources in shear zones, Zhang et al. [9] and Liang et al. [10] have proposed analytical models aimed at predicting surface integrity. These physics-based models offer deeper insights into how different parameters influence internal loads and the resulting surface integrity.

Through finite element modeling, Chen et al. [11] provide key insights into the effects of increasing the edge radius on the evolution of stagnation point height. However, Lagrangian simulations struggle with element distortion and tool-tip contact management. For these reasons, hybrid modeling approaches, such as those introduced by Valiorgue et al. [12] and further developed by Dumas et al. [13], address these issues more effectively. However, these models have limitations in experimental data utilization, as experimental results serve primarily as corrective factors for identifying equivalent loads on the final surface.

In light of this, the present article proposes a chipless hybrid numerical modeling method that integrates experimental forces as input data for calculating thermal sources, and determines the temperature field on the workpiece during the cutting operation. This approach aims to improve the understanding of how external thermo-mechanical loads from various edge microgeometries influence temperature fields within the workpiece.

2. Experimental setup

2.1. General setup

To measure forces and temperature fields below the final surface for various tool microgeometries, the experimental setup shown in Fig. 1 was implemented. This setup was realized by linearly operating the x-axis of a DMG DMC85V 3-axis machine tool, with a 2 mm width (b) Ti-6Al-4V α+β titanium sample clamped on it by the mean of a specific device. The use of a stationary tool, enables the measurement of the thermal field throughout the cutting process with an Eulerian point of view. The workpiece was clamped in a square, which was itself fixed on the spindle. An ARNO ISO K20 carbide insert, with a rake angle $\gamma = 20$ ° and a clearance angle $\alpha = 12$ °, was mounted on a tool holder with a 5 ° inclination angle (λ_s) to prevent burr formation ahead of the camera's view. The holder was then clamped to a Kistler 9119AA2 piezoelectric dynamometer. Through horizontal displacement of the x-axis at a cutting speed of $v_c = 40$ *m/min*, orthogonal cutting was performed, and the temperature field was observed using a Telops MS-M3k infrared. To estimate the real chip thicknesses removed, a scan of the sample's upper surface was performed before and after each pass using a Keyence LK-G32 point laser.

For each tool microgeometry, three chip thicknesses of $h_{command} = 0.01/0.02/0.06$ *mm* were cut, with each pass repeated three times, resulting in nine tests per cutting edge. Preliminary clearing passes were conducted with each change in chip

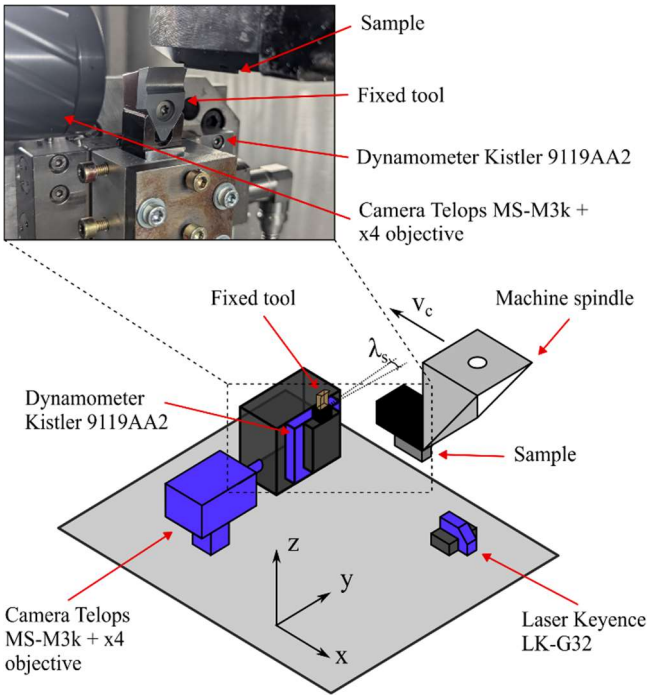

Fig. 1. Schematic view of the experimental setup

thickness or microgeometry. Three types of tool microgeometries were tested: honed edges (Fig. 2. (a)), chamfered on the rake face (Fig. 2. (b)), and chamfered on the clearance face to simulate flank wear (Fig. 2. (c)). They were chosen to influence the position of the stagnation point, and the tool/workpiece contact length. Their geometric characteristics are given in Fig. 2.

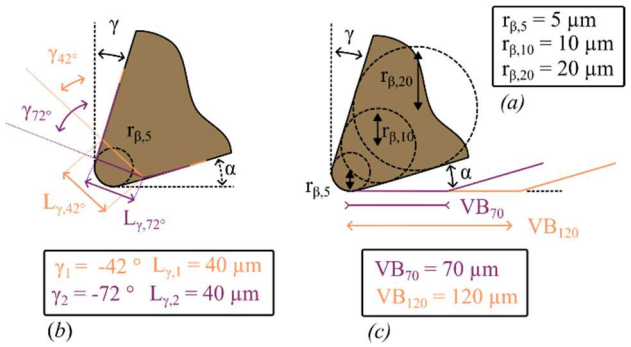

Fig. 2. Schematic view and definition of the tested too microgeometries *(a)* Rounded *(b)* Chamfered *(c)* Artificially worn

2.2. Infra-red camera setup and calibration

To determine the temperature field generated on the final surface during the operation, the radiance of each pixel in the scene is measured using a Telops MS-M3k infrared camera. The measurement parameters are provided in Table 1. To optimize the accuracy of the measurements, the observed surface of the samples was mirror-polished and coated with a nickel deposit to increase the emissivity. The specimens were then placed in an oven heated at 200°C, 250°C, and 300°C, and their radiance were measured. By knowing the average radiance of the scene as well as its temperature, the emissivity of the specimen was determined through an inverse method. An emissivity of $\varepsilon = 0.600 \pm 0.003$ has been determined

inducing an error inferior to 5°C on the calculated temperature as suggested by Poissenot et al. [14].

Table 1. Infrared camera measurement parameters

Sensor type	lnSb
Spectral range	3.11 – 5.50 µm
Spatial resolution	7.5 µm/pixel
Scene size	2.4 x 1.92 mm
Acquisition frequency	700 Hz
Integration time	27 µs

3. Modeling methodology

3.1. Cutting law identification

To determine the variation of the process forces as a function of the uncut chip thickness and to separate the forces generated by cutting and ploughing phenomena, an Armarego cutting law [15] was chosen and is given in Eq. 1. This model offers advantages over power-law or fractional law [16], notably by providing a phenomenological partition between chip formation and edge forces, which will be used in the numerical modeling.

$$\begin{cases} F_c = \left(K_{ch,c}.h + K_{edge,c}\right).b = F_{ch,c} + F_{edge,c} \\ F_t = \left(K_{ch,t}.h + K_{edge,t}\right).b = F_{ch,t} + F_{edge,t} \end{cases} \quad (1)$$

To conduct the identification of the cutting law coefficients, the measured chip thicknesses $h_{measured}$ were used. The forces monitored during each trial via the dynamometer were averaged along the pass. And Similarly, for the uncut chip thicknesses, the difference in upper surfaces position, before and after cutting, was calculated and then averaged. To enhance the reliability of the cutting law identification, a linear regression was made on the averaged forces and uncut chip thicknesses of the repeated passes. The cutting law identifications for 3 representative microgeometries are given in Fig. 3.

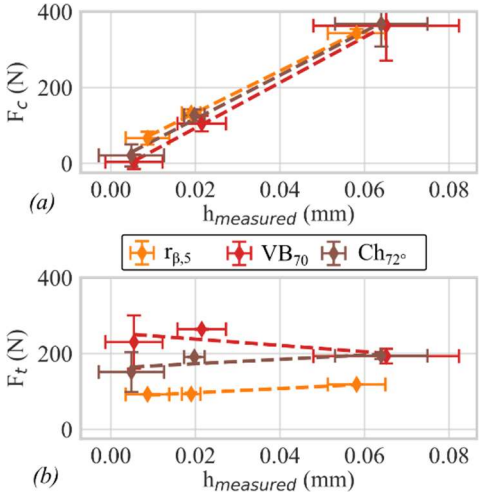

Fig. 3. Correlation of *(a)* $h_{measured}$ and $h_{command}$ *(b)* $h_{measured}$ and the cutting forces

3.2. Analytical calculation of the external thermal sources

In accordance with Albrecht's force partitioning model [17], the current modeling approach separates forces associated with chip formation from those related to tool microgeometry effects (Fig. 4 (a) (b)). It is done by the superposition of a Merchant cutting configuration (Fig. 4 (c)) and a friction model representing a flat rigid solid sliding on a planar surface (Fig. 4 (d)). Thus, the heat fluxes generated within the different shear zones are analytically calculated based on experimental data. For the cutting configuration, the heat flux density in the Primary Shear Zone (PSZ) is calculated using Eq. 2.

$$q_{PSZ} = \frac{F_{ch,s}.v_s}{A_s} \quad (2)$$

With q_{PSZ} the heat flux density in the PSZ, $F_{ch,s}$ the shear force derived from Merchant's model [18] and given by Eq.3, v_s the shear speed obtained by the projection of v_c in Eq. 4 and A_s the surface of the shear band given in Eq. 5.

$$F_{ch,s} = F_{ch,c}.cos(\phi) - F_{ch,t}.sin(\phi) \quad (3)$$

With ϕ the shear angle.

$$v_s = \frac{v_c.cos(\gamma)}{cos(\phi - \gamma)} \quad (4)$$

$$A_s = \frac{b.h}{sin(\phi)} \quad (5)$$

In the Secondary Shear Zone (SSZ), the heat flux density is given by Eq. 6.

$$q_{SSZ} = \frac{F_{t,\gamma}.v_{ch}}{b.L_\gamma} \quad (6)$$

With q_{SSZ} the heat flux density in the SSZ, $F_{t,\gamma}$ the tangential force on the rake face given by Eq. 7, v_{ch} the chip speed in Eq. 8 and L_γ the chip/tool contact length given by Oxley [19] in Eq. 9

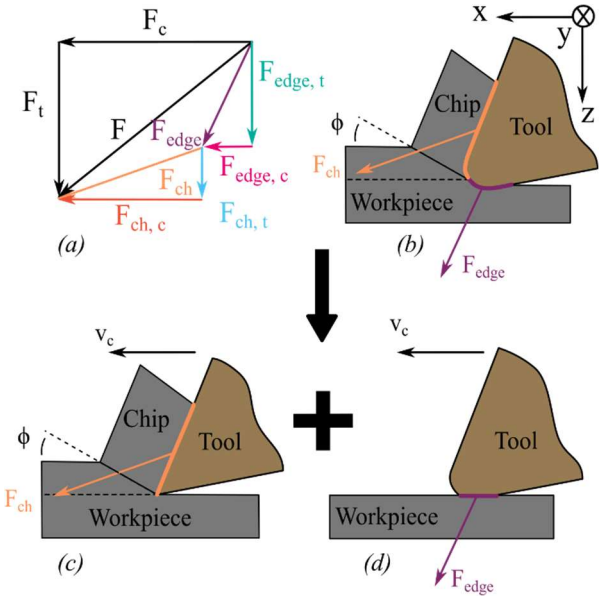

Fig. 4. *(a)* Cutting forces description *(b)* Schematic view of the partition *(c)* Chip formation configuration *(d)* Edge friction configuration

by assuming a constant stress-state along the tool-chip interface.

$$F_{t,\gamma} = F_{ch,c}.sin(\gamma) + F_{ch,t}.cos(\gamma) \quad (7)$$

$$v_{ch} = \frac{v_c.sin(\phi)}{cos(\phi - \gamma)} \quad (8)$$

$$L_\gamma = h.\frac{sin(\beta_{ch})}{sin(\phi).sin(\phi + \beta_{ch} - \gamma).cos(2.(\phi - \gamma))} \quad (9)$$

Where β_{ch} is the mean friction angle on the rake face given by Eq. 10.

$$\beta_{ch} = \gamma + tan^{-1}\left(\frac{F_{ch,t}}{F_{ch,c}}\right) \quad (10)$$

Consequently, the assumptions are those of Merchant's model: a continuous orthogonal cutting configuration with a perfectly sharp cutting edge, no clearance face contact, no built-up edge formation, and a perfectly plastic material. The continuous cutting assumption is made as a first approximation given that the experimental forces are averaged along the pass. Moreover, as suggested by Li et al. [20], high cutting angles and low cutting speeds tend to reduce chip segmentation angle.

In addition, the Tertiary Shear Zone (TSZ) is modeled using a plane Coulomb friction configuration, which implies a linear relationship between the forces in the cutting and thrust directions as described in Eq. 11. Thus, a uniform distribution of forces and velocity is assumed along the tool/workpiece contact interface.

$$tan(\beta_{edge,app}) = \frac{F_{edge,t}}{F_{edge,c}} \quad (11)$$

With $\beta_{edge,app}$ the mean apparent friction angle of the edge sliding on the final surface. The heat flux density in the TSZ is then similarly described in Eq. 12.

$$q_{TSZ} = \frac{F_{edge,c}.v_c}{b.L_\alpha} \quad (12)$$

Where L_α is the tool/workpiece contact length. The contact lengths for the various microgeometries are obtained with a post-cutting observation of the insert with a numerical microscope Alicona InfiniteFocusSL by differentiating the worn and unused area on the clearance face.

3.3. Eulerian heat balance

Assuming continuous cutting for the calculation of thermal sources, the problem can be modeled as shown in Fig. 5 (a), adopting an Eulerian perspective rather than the commonly used Lagrangian point of view. In this approach, the tool is considered stationary, with a material flow moving around its boundaries. Since Abaqus/Standard does not natively support solving such problems, a Field Transfer (FT) model was used. The operational flowchart of this model is illustrated in Fig. 5 (c). The assumptions of an adiabatic model, infinite tool and workpiece, and perfect contact between the tool, chip, and workpiece are made. Concerning the Finite Element (FE) model generated for each FT increment and illustrated in

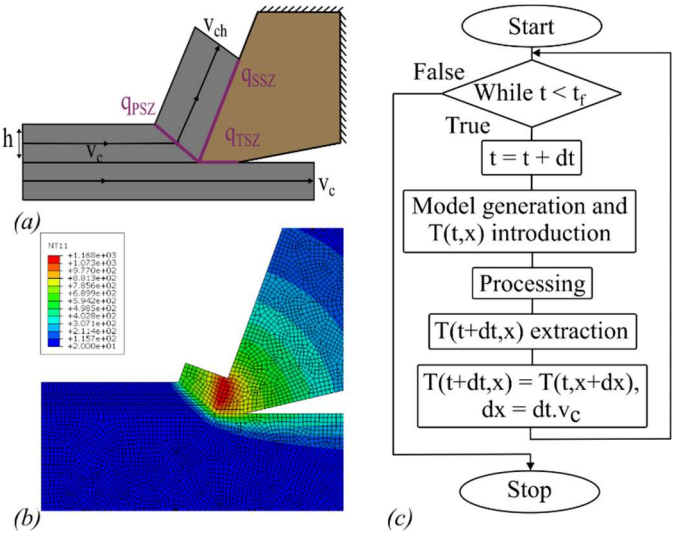

Fig. 5. *(a)* Schematic Eulerian modeling *(b)* Model flowchart *(c)* FE model illustration

Fig. 5 (b), a single solid is defined with different material assignments, using the thermal properties of Ti-6Al-4V and carbide WC-CO detailed in Table. 2. The shear zones are specified as elements sets so that thermal loads can be applied on the model's internal boundaries using body heat fluxes. The initial temperature fields for each simulation at time *dt* are introduced via a predefined field extracted from the previous step and translated by *dx*. The elements used are of type DC2D4, and their sizes are selected in alignment with the chosen time step. Indeed, it is necessary that the characteristic penetration depth of the thermal conduction corresponds to the translation increment *dx* applied to the extracted temperature field. This requirement is described by Eq. 13.

$$dt = \frac{dx}{v_c} = \frac{seedMesh^2}{\alpha_{TA6V}} \quad (13)$$

With *seedMesh* the length of a mesh element that correspond to the thermal penetration depth and α_{TA6V} the thermal diffusivity of Ti-6Al-4V given by Eq. 14.

$$\alpha_{TA6V} = \frac{\lambda_{TA6V}}{\rho_{TA6V}.c_{p,TA6V}} \quad (14)$$

Table 2. Test matrix

ρ_{TA6V} (t/mm^3)	λ_{TA6V} (mW/mm/K)	$c_{p,TA6V}$ (mJ/t/K)	ρ_{WC-CO} (t/mm^3)	λ_{WC-CO} (mW/mm/K)	$c_{p,WC-CO}$ (mJ/t/K)
4.43E-9	6.70	560E6	1.57E-8	24.0	178E6

4. Results and discussions

4.1. Influence of the tool microgeometry on the external thermo-mechanical loads

The influence of different microgeometries on external thermo-mechanical loads, is shown in Fig. 6 for an uncut chip thickness of $h_{command} = 0.06\ mm$. Cutting coefficients exhibit

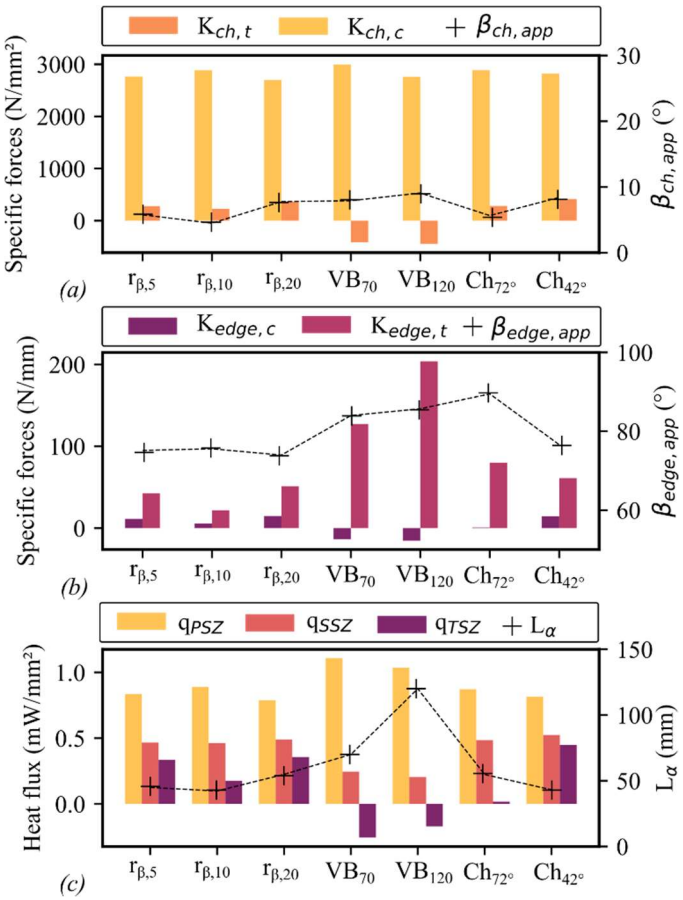

Fig. 6. Comparison for $h_{command} = 0.06$ *mm* of *(a)* Specific cutting forces *(b)* Specific edge forces *(c)* Thermal sources calculated

minimal variations, highlighting the impact of microgeometries on heat flux densities. Edge coefficients significantly increase between $r_{\beta,10}$ and $r_{\beta,20}$ due to greater ploughed material volume. Elevated forces for the $r_{\beta,5}$ result from premature micro-chipping, a common wear behavior for titanium/carbide pairs. Chamfered edges show higher thrust forces and friction coefficients, with $Ch_{42°}$ comparable to $r_{\beta,20}$ and $Ch_{72°}$ matching VB geometries. At small chip thicknesses, tool flexion increases thrust forces until stabilization occurs, explaining the negative coefficients seen for VB_{70} in Fig. 3. Consequently, PSZ thermal flux amplitudes show minor variations, while TSZ fluxes align with edge specific forces trends.

4.2. Experimental validation

To validate the modeling method, numerical and experimental temperature fields beneath the final surface were compared. The simulation results were cubic-interpolated onto the pixel grid of the camera and restricted to its filter temperature range. The comparison of the two temperature fields obtained for $r_{\beta,5}$ with an uncut chip thickness of $h_{command} = 0.06$ *mm* is illustrated in Fig. 7. A mean error of 44 °C is obtained between the two surfaces and the shape concordance suggests good agreement, with a Pearson and Spearman correlation coefficients of 0.85 and 0.84, respectively. This indicates a linear correlation between the two surfaces. The complete statistical comparison of the temperature fields for the various tests is provided in Table. 3. The mean errors and correlation coefficients show similar

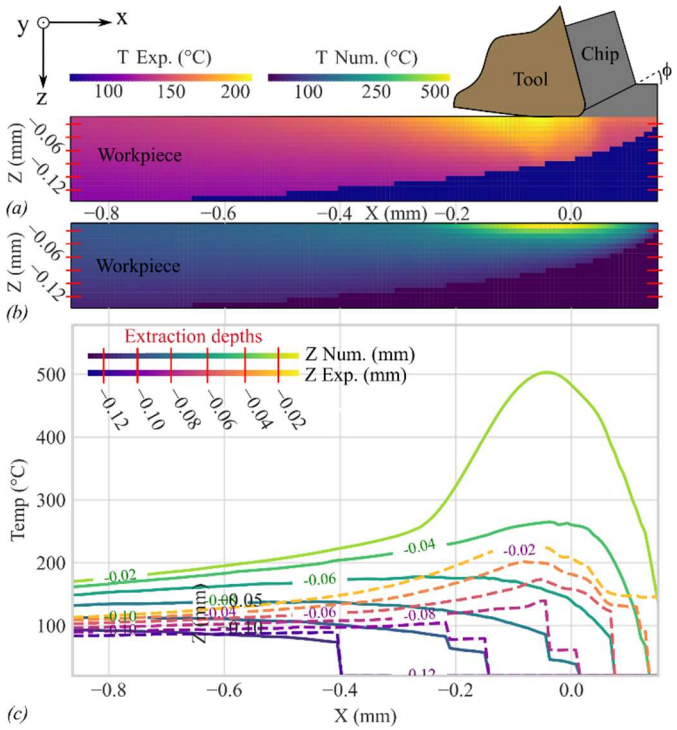

Fig. 7. *(a)* Numerical and *(b)* Experimental thermal fields for $r_{\beta,5}$ and $h_{command} = 0.06$ *mm*. *(c)* Their profiles comparison through depth

trends across all tested microgeometries. These mismatches likely came from consistent factors, including overestimated thermal sources due to omitted efficiency factors (*e.g.*, the Taylor-Quinney coefficient) or limitations in using the Armarego cutting law for small chip thicknesses. Moreover, the low spatial resolution of the measurements amplifies errors near the final surface.

Table 3. Statistical comparison of the thermal's fields for the different microgeometries and chip thicknesses

	Mean error (°C)			Pearson (/)			Spearman (/)		
h	0.01	0.02	0.06	0.01	0.02	0.06	0.01	0.02	0.06
$r_{\beta,5}$	19	28	45	0.83	0.79	0.84	0.86	0.79	0.82
$r_{\beta,10}$	26	13	41	0.84	0.85	0.85	0.91	0.89	0.84
$r_{\beta,20}$	27	52	42	0.87	0.82	0.88	0.93	0.95	0.86
VB_{70}	23	19	59	0.88	0.84	0.89	0.87	0.87	0.88
VB_{120}	14	27	31	0.85	0.88	0.56	094	0.88	0.85
$Ch_{..72°}$	36	30	21	0.91	0.89	0.95	0.95	0.92	0.94
$Ch_{..42°}$	23	24	32	0.90	0.81	0.55	0.90	0.87	0.78

4.3. Influence of the tool microgeometry on the thermal state of the workpiece

Temperature profiles at a depth of 45 µm beneath the final surface from both experimental and numerical fields are shown in Fig. 8. To numerically study flank wear effects on the temperature field, specific forces for the VB configurations were normed. Maximum errors occur at the peaks of the temperature curves, but the ranking order among microgeometries within the same family remains consistent between numerical and experimental results. The lowest

temperature is observed for the lowest edge radius tool $r_{\beta,10}$, while configurations VB_{70}, $r_{\beta,5}$ and $r_{\beta,20}$ generate similar temperatures. VB_{120} also generates more heat than VB_{70}. Thus, heat generation increase with larger edge radii or greater flank wear, primarily influenced by the TSZ. Significant deviations for chamfered edges are attributed to poor edge-specific force identification. Larger VB extends contact length and friction at the flank, increasing edge forces and heat generated. Similarly, larger edge radii increase the stagnation point height and contact length, intensifying heat generated from friction and tool-tip deformation. Chamfers reduce the tool-tip cutting angle, altering cutting mechanics based on the chamfer angle.

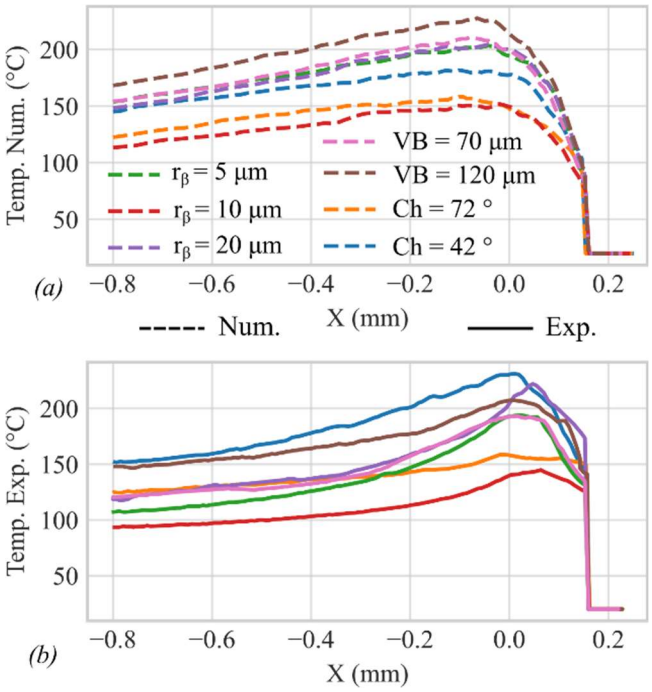

Fig. 8. *(a)* Numerical and *(b)* Experimental temperature profiles for $h_{command} = 0.06$ *mm* at 45 µm beneath machined surface

5. Conclusion and perspectives

The study presented here introduces a novel hybrid chipless modeling methodology to analyze and predict temperature fields generated in the workpiece for various tool microgeometries. This approach relies on the identification and partitioning of forces arising from chip formation and tool microgeometry. These data are used to compute the external thermal loads generated in the shear zones, enabling a heat balance to be conducted using a FT model. A comparison between numerical and experimental temperature fields is performed, followed by an investigation of the influence of different tool microgeometries on sub-surface temperature. The mismatches observed suggest that the methodology holds promise, while the trends indicate an increase in generated heat with larger edge radii or longer flank contact lengths.

The proposed model has limitations for non-circular microgeometries, as the use of an Armarego cutting law with constant edge-related forces oversimplifies the phenomena involved. Cutting regimes, such as friction, ploughing, variable rake angle cutting, and constant rake angle cutting, vary with the microgeometry and uncut chip thickness. These regimes significantly affect heat generation and evacuation. Thus, an accurate temperature field prediction using a hybrid chipless method requires a detailed description of cutting forces and regimes. This capability could enable reliable predictions of machining-induced surface integrity modifications.

Acknowledgements

The authors would like to thank AIRBUS Operations SAS for funding this work, and Rayen Hanna for the technical support.

References

[1] Denkena B, Biermann D, Cutting edge geometries. CIRP Annals 2014
[2] Zhuang K, Fu C, Weng J, Hu C Cutting Edge Microgeometries in Metal Cutting: A Review. Int J Adv Manuf Technol 2021
[3] Wyen CF,Wegener K, Influence of cutting edge radius on cutting forces in machining titanium, CIRP Annals 2010
[4] Segebade E, Kümmel D, Zanger F, Schneider J, Schulze V Influence of cutting edge asymmetry on grain refinement of Ti6Al4V. Procedia CIRP 2018
[5] Denkena B, Lucas A, Bassett E Effects of the cutting edge microgeometry on tool wear and its thermo-mechanical load, CIRP Annals 2011
[6] M'Saoubi R, Chandrasekaran H, Investigation of the effects of tool micro-geometry and coating on tool temperature during orthogonal turning of quenched and tempered steel, Int J Mach Tool Manu 2004
[7] Waldorf DJ, DeVor RE, Kapoor SG A slip-line field for ploughing during orthogonal cutting. J Manuf Sci E T ASME 120 1998
[8] Komanduri R, Hou ZB, Thermal modeling of the metal cutting process: Part I — Temperature rise distribution due to shear plane heat source, Int J Mech Sci 2000
[9] Zhang WQ, Wang XL, Hu YJ, Wang SY Predictive modelling of microstructure changes, micro-hardness and residual stress in machining of 304 austenitic stainless steel. Int J Mach Tool Manu 2018
[10] Liang X, Liu Z, Wang B, Song Q, Cai Y, Wan Y Prediction of Residual Stress with Multi-Physics Model for Orthogonal Cutting Ti-6Al-4V under Various Tool Wear Morphologies. J Mat Process Technol 2021
[11] Chen G, Caudill J, Ren C, Jawahir IS Numerical modeling of Ti-6Al-4V alloy orthogonal cutting considering microstructure dependent work hardening and energy density-based failure behaviors, J Manuf Process 2022
[12] Valiorgue F, Rech J, Hamdi H, Gilles P, Bergheau J M. A New Approach for the Modelling of Residual Stresses Induced by Turning of 316L. J Mat Process Techno 2007
[13] Dumas M, Fabre D, Valiorgue F, Kermouche G, Robaeys AV, Girinon M, Brosse A, Karaouni H, Rech J, 3D Numerical Modelling of Turning-Induced Residual Stresses – A Two-Scale Approach Based on Equivalent Thermo-Mechanical Loadings. J Mat Process Techno 2021
[14] Poissenot-Arrigoni C, Marcon B, Rossi F, Fromentin G, In-Situ Pixel-wise Emissivity Measurement Using a Multispectral Infrared Camera. J. Imaging, 2023
[15] Armarego EJA, Brow E, The machining of metals, Prentice Hall Inc, Englewood Cliffs, NJ 1969
[16] Paris H, Brissaud D, Gouskov A, A more realistic cutting force model at uncut chip thickness close to zero. CIRP annals 2007
[17] Albrecht P, New Developments in the Theory of the Metal-Cutting Process: Part I. The Ploughing Process in Metal Cutting, ASME. J. Eng. Ind, 1960
[18] Merchant ME, Mechanics of the metal cutting process I, J. Appl. Phys., 1945
[19] Oxley PL, An analysis for orthogonal cutting with restricted tool-chip contact. Int J Mech Sci, 1962
[20] Li A, Zang J, Zhao J, Effect of cutting parameters and tool rake angle on the chip formation and adiabatic shear characteristics in machining Ti-6Al-4V titanium alloy. Int J Adv Manuf Technol 2020